Design and Optimization of an Ultra Wideband and Compact Microwave Antenna for Radiometric Monitoring of Brain Temperature

Dario B. Rodrigues*, *Student Member, IEEE*, Paolo F. Maccarini, *Member, IEEE*, Sara Salahi, Tiago R. Oliveira, Pedro J. S. Pereira, Paulo Limão-Vieira, Brent W. Snow, Doug Reudink, *Life Fellow, IEEE*, and Paul R. Stauffer, *Member, IEEE*

***Abstract*—We present the modeling efforts on antenna design and frequency selection to monitor brain temperature during prolonged surgery using noninvasive microwave radiometry. A tapered log-spiral antenna design is chosen for its wideband characteristics that allow higher power collection from deep brain. Parametric analysis with the software HFSS is used to optimize antenna performance for deep brain temperature sensing. Radiometric antenna efficiency (η) is evaluated in terms of the ratio of power collected from brain to total power received by the antenna. Anatomical information extracted from several adult computed tomography scans is used to establish design parameters for constructing an accurate layered 3-D tissue phantom. This head phantom includes separate brain and scalp regions, with tissue equivalent liquids circulating at independent temperatures on either side of an intact skull. The optimized frequency band is 1.1–1.6 GHz producing an average antenna efficiency of 50.3% from a two turn log-spiral antenna. The entire sensor package is contained in a lightweight and low-profile 2.8 cm diameter by 1.5 cm high assembly that can be held in place over the skin with an electromagnetic interference shielding adhesive patch. The calculated radiometric equivalent brain temperature tracks within 0.4 °C of the measured brain phantom temperature when the brain phantom is lowered 10 °C and then returned to the original temperature (37 °C) over a 4.6-h experiment. The numerical and experimental results demonstrate that the optimized 2.5-cm log-spiral antenna is well suited for the noninvasive radiometric sensing of deep brain temperature.**

***Index Terms*—Antenna design, brain temperature, log-spiral antenna, microwave radiometry, noninvasive monitoring.**

I. Introduction

PROLONGED surgeries use general anesthesia that impairs thermoregulation processes in the human body and is associated with hypothermia, i.e., when core temperature is below 36 °C [1]. In some surgeries, hypothermia is actually forced; patients are cooled 5–18 °C below normal body temperature in order to reduce the sensitivity of critical brain tissues to ischemia [2]. In either case, it is critical to safely and rapidly rewarm the patient to normal body core temperature (37 °C) before the end of surgery to avoid complications such as a higher risk of morbid myocardial outcomes or prolonged surgical recovery [1]–[4]. Current thermometry devices typically measure surface temperatures or intracavitary surrogates of body temperature that do not accurately reflect true core temperature of deep organs. Each of these core temperature surrogates have inherent problems with probe placement, time delay in readings, and/or are objectionably invasive [5], [6]. In this paper, we present a novel monitoring approach based on noninvasive and entirely passive microwave (MW) radiometry. We choose to monitor core temperature inside the brain rather than in alternative sites due to the critical nature of this organ and its central role in thermoregulation [2], [7], [8].

MW radiometry is a noninvasive technique that collects thermal radiation (electromagnetic noise) emitted in the MW frequency spectrum by any material above absolute zero temperature. The thermal radiation is received by an antenna and converted, with proper calibration, into a measure of absolute temperature taken from a weighted average of its radiation pattern [9]–[11]. This technique contrasts with infrared thermometry that collects thermal radiation at higher frequencies (0.3–430 THz), where photons travel only a few millimeters through skin.

There have been many reports of medical applications of MW radiometry, including the detection of breast cancer [12], monitoring and control of superficial and deep hyperthermia applicators [13]–[15], measurement of brain temperature in infants [9]

Manuscript received November 28, 2013; revised March 9, 2014; accepted April 9, 2014. Date of publication April 15, 2014; date of current version June 14, 2014. This work was supported by NIH R21-DK092912 and Thermimage Corp. The work of D. B. Rodrigues was supported by the Portuguese Foundation for Science and Technology through the Postgraduate Scholarship SFRH/BD/73215/2010. The work of D. B. Rodrigues, P. J. S. Pereira, and P. Limão-Vieira was supported by the Portuguese Foundation for Science and Technology under Grant PEstOE/FIS/UI0068/2011. *Asterisk indicates corresponding author.*

*D. B. Rodrigues is with the Centre of Physics and Technological Research, Universidade Nova de Lisboa, 2829-516 Caparica, Portugal (e-mail: db.rodrigues@campus.fct.unl.pt).

P. F. Maccarini, S. Salahi, and P. R. Stauffer are with the Department of Radiation Oncology, Duke University, Durham, NC 27710 USA (e-mail: paolo.maccarini@duke.edu; sara.louie@ansys.com; paul.stauffer@duke.edu).

T. R. Oliveira is with the Physics Institute, University of São Paulo, 05508-090 São Paulo, Brazil (e-mail: tiagor@if.usp.br).

P. J. S. Pereira is with the Department of Mathematics, Instituto Superior de Engenharia de Lisboa, 1959-007 Lisboa, Portugal (e-mail: ppereira@deq.isel.ipl.pt).

P. Limão-Vieira is with the Centre of Physics and Technological Research, Universidade Nova de Lisboa, 2829-516 Caparica, Portugal (e-mail: plimaovieira@fct.unl.pt).

B. W. Snow is with the Department of Surgery and Urology, University of Utah, Salt Lake City, UT 84113 USA (e-mail: brent.snow@hsc.utah.edu).

D. Reudink is with ThermImage, Salt Lake City, UT 84127 USA (e-mail: dougr@thermimage.com).

Color versions of one or more of the figures in this paper are available online at http://ieeexplore.ieee.org.

Digital Object Identifier 10.1109/TBME.2014.2317484

or adults [16], vesicoureteral reflux detection in young children [17], [18] and more recently monitoring of brown fat metabolism [19]. In the particular case of monitoring adult brain temperature, there are no reports to our knowledge of an antenna that is small enough to conform to the human head during prolonged surgery, present a stable reading over several hours, and offer an accuracy below 0.5 °C, which is the smallest difference that has been associated with hypothermia-induced complications [7].

The major challenge in MW radiometry lies in the nature of thermal noise itself which is characterized by extremely low-power levels ($\sim 10^{-14}$ W/MHz at 37 °C). To maximize power collection, wideband antennas are generally used to collect thermal noise over a wide frequency range. We previously demonstrated that due to its circular polarization and wideband matching, a 7-cm-diameter log-spiral antenna is sensitive to small temperature variations in deep-seated targets [17]. Thus, we choose the same log-spiral design for our new compact radiometric sensor, but in order to be conformal with the human head, we use a diameter of 2.5 cm.

In this paper, we focus on the theoretical modeling of the design of a miniature 2.5-cm-diameter receive antenna and optimization of the frequency band for radiometric temperature monitoring of brain. A realistic head phantom model is built to validate the theory and demonstrate performance of this sensor.

II. Material and Methods

A. Log-Spiral Antenna Design

Log-spiral antennas exhibit frequency-independent properties over a wideband limited by the finite physical dimensions of the antenna [20], [21]. The microstrip log-spiral design explored in this study consists of a single arm with variable width metal trace formed by ρ_{e0} (inner) and ρ_{e1} (outer), defined by

$$\begin{cases} \rho_{e0} : \rho = \rho_0 e^{a\theta} \\ \rho_{e1} : \rho = \rho_1 e^{a\theta} \end{cases} \tag{1}$$

where (ρ, θ) are polar coordinates; $\rho_0 = 0.25$ mm and $\rho_1 = 0.75$ mm are the initial ($\theta = 0$) inner and outer radius of the metal trace, respectively, located at the center of a coaxial feed port with diameter $\rho_1 - \rho_0$; and a is the spiral growth rate coefficient given by $a = \ln(\rho_{\text{ext}}/\rho_0)/(2\pi N)$, which is defined by the number of log-spiral turns (N) possible within an outer radius (ρ_{ext}). The antenna diameter is fixed at 2.5 cm to allow the sensor to be conformal with the human head. The end of the spiral arm is tapered (see Fig. 1) to minimize reflections at lower frequencies and improve impedance matching [21].

Since the function of the antenna is to collect thermal radiation, which is randomly polarized, it is desirable for the antenna to have circular or elliptical rather than linear polarization. When the antenna arm length is shorter than one wavelength, polarization is linear. As the arm length is increased (or frequency increased), the polarization becomes nonlinear [20]. To be an efficient radiator, the spiral length must be at least similar to the wavelength. Thus, the number of turns is a parameter to be optimized. The arm length $L(N)$ is determined over the line

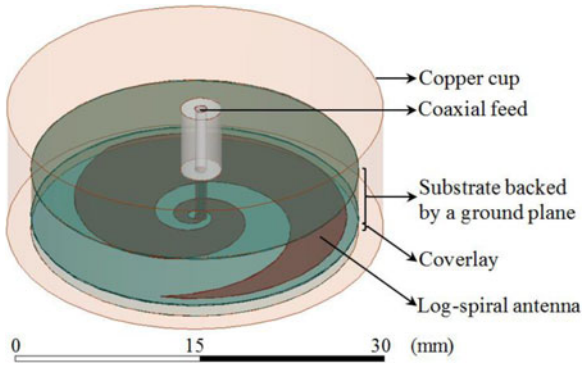

Fig. 1. Radiometric receive antenna: microstrip log-spiral patch design with tapered ends.

TABLE I
Ceramic Substrates Used in the Antenna Design

Substrate	Permittivity ε_r	Conductivity σ (S/m)
RO3003©	3.00	2.93×10^{-4}
RO3006©	6.15	9.23×10^{-4}
RO3010©	10.20	1.68×10^{-3}

defined by ρ_{e0} and is given by

$$L(N) = (\rho_{\text{ext}} - \rho_0)\sqrt{1 + a(N)^2}/a(N). \tag{2}$$

The microstrip is mounted on a 4.45-mm-thick hydrocarbon ceramic substrate that is backed by a ground plane (Fig. 1). Three different substrates are chosen from the RO3000 series (Rogers Corp., Rogers, CT, USA) due to availability, ease of construction, high dielectric permittivity, and ultralow loss properties (see Table I), all of which are desirable for radiometric applications.

The presence of a very thick and high dielectric substrate behind the antenna will affect the antenna's operating bandwidth. According to the *ring theory* [22], the lower cutoff frequency f_L is a function of the circumference length with radius ρ_{ext} and the higher cutoff frequency f_H is dependent on the diameter of the coaxial feed port (ρ_1–ρ_0):

$$\begin{cases} f_H = c\Big/\left(2\pi(\rho_1 - \rho_0)\sqrt{\varepsilon_{r,\text{eff}}}\right) \\ f_L = c\Big/\left(2\pi\rho_{\text{ext}}\sqrt{\varepsilon_{r,\text{eff}}}\right) \end{cases} \tag{3}$$

where c is the speed of light and $\varepsilon_{r,\text{eff}}$ is the effective permittivity, which affects the wavelengths detected by the antenna.

The final element of the antenna is a thin coverlay disk (radius ρ_{ext}) placed between the spiral metal trace and scalp (see Fig. 1), which is used to improve antenna match impedance to tissue and provide electrical insulation of the metal from the conductive skin. The coverlay is chosen from the ultralow loss ($\sigma_{\text{coverlay}} = 4.50 \times 10^{-3}$ S/m) Eccostock HiK series (Emmerson & Cumming, Randolph, MA, USA) with thickness (δ) and dielectric permittivity to be optimized (see Table II).

B. Experimental Human Head Phantom Model

A physical head phantom was developed to validate the optimized antenna design. From computed tomography (CT) scans of an unidentified patient head, we determined appropriate

TABLE II
LOG-SPIRAL ANTENNA PARAMETERS FOR PARAMETRIC ANALYSIS

Property	Parametric analysis
Coverlay permittivity $\varepsilon_{r,coverlay}$	5-40 with step = 5
Log-spiral turns N	0.25-2.75 with step = 0.25
Coverlay thickness δ (mm)	0–5 mm with step = 1 mm

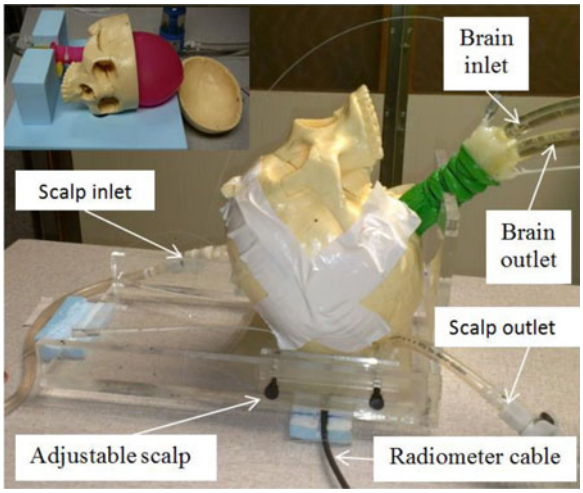

Fig. 2. Human head model with variable temperature liquid brain phantom. This liquid circulates through a balloon that fills the inside of the skull. The liquid scalp phantom is also temperature controlled and circulates in an adjustable thickness region under the skull. The black coaxial cable connects the radiometer electronics to the antenna sensor coupled to scalp surface.

values for the thickness of scalp, bone, and brain tissues to generate a realistic physical model. Measurements showed that scalp thickness varies from 4.2 (forehead) to 8 mm (temporal lobe), and the average thickness of skull bone is 6.7 mm in both regions. Based on these dimensions, an experimental model of the human head was constructed (see Fig. 2) around an artificial human skull (Life Size Skull, www.anatomywarehouse.com).

To model the thermodynamics of scalp, an adjustable thickness (6–16 mm) compartment filled with circulating temperature-controlled distilled water was sealed against the outer surface of the skull. A mixture of propylene glycol (46%) and deionized water (54%) was used to approximate the electrical properties of mixed grey and white matter. The brain liquid phantom was circulated vigorously (1.7 L/min) with a high flow peristaltic pump (Masterflex 7592-40, Cole Parmer, Vernon Hills, IL, USA) through a water bath heater (Neslab RTE740, Cole Parmer) and into a latex balloon (see Fig. 2, top left) that filled the interior of the skull. Scalp temperature was circulated similarly, but controlled in a different water bath to allow independent scalp and brain temperatures and thus obtain realistic differential temperature of surface and deep tissues.

Electrical properties for the liquid tissue phantoms were characterized at normothermic temperatures for scalp (32 °C) and brain (37 °C) using a coaxial dielectric probe (E85070C, Agilent Technologies, Santa Rosa, CA, USA) connected to a network analyzer (E5071C, Agilent Technologies).

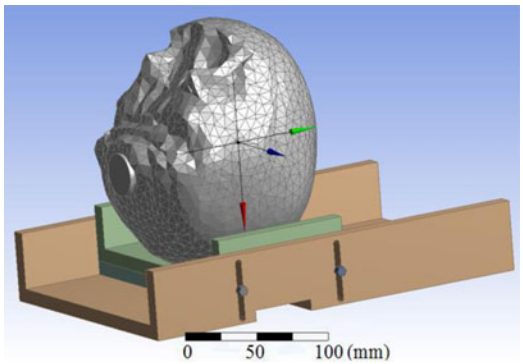

Fig. 3. Computational model of the multilayer human head phantom used for antenna optimization.

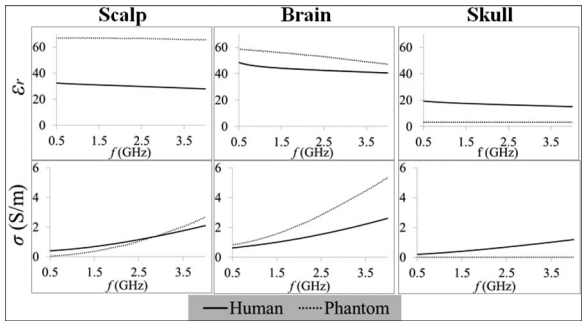

Fig. 4. Frequency-dependent electrical properties (relative permittivity ε_r and electrical conductivity σ) of both phantom models (measured here) and human tissues [23].

C. Virtual Human Head Computational Model

The physical head phantom was translated into an anatomically accurate computer-aid design model (see Fig. 3). CT images of the artificial skull were acquired and segmented using Avizo (Visualization Sciences Group, Burlington, MA, USA). The resulting 3-D surfaces of the surrogate skull were assumed to be the outer boundary of a uniform volume of tissue. The remaining objects were created in DesignModeler (Ansys Inc., Canonsburg, PA, USA) with accurate geometry and dimensions. The final virtual phantom model was then imported into HFSS (Ansys Inc., Canonsburg, PA, USA) and coupled with the antenna design to perform a finite element method simulation-based optimization. This computational approach has been validated experimentally for similar antenna design projects [18], [19]. Note that the phantom frequency-dependent properties were integrated in this dispersive numerical model (see Fig. 4).

D. Optimization Goals

The reciprocity theorem states that the radiation and receiving patterns of an antenna are identical [10]. Thus, one can estimate the radiation receiving pattern from the power loss density profile $P_d(\mathrm{W/m^3})$ that is given by

$$P_d(\boldsymbol{r}) = \frac{1}{2}\sigma\,|\boldsymbol{E}(\boldsymbol{r})|^2 \tag{4}$$

TABLE III
LOG-SPIRAL ANTENNA GOAL FUNCTIONS AND CONSTRAINTS

Function	Goal/Constraints
Efficiency η	Maximization
Bandwith Δf	Maximization
S_{11}	$\leq$ -10 dB
FCC allocated frequencies	0.81-0.96, 1.71-1.99, and 2.4-2.5 GHz

where $\boldsymbol{E}$ (V/m) is the electric field at the position $\boldsymbol{r}$ in the computational domain V. The antenna efficiency η is evaluated in terms of P_d and is defined by the ratio of power received from brain to total power received by the antenna:

$$\eta = \frac{\int_{V_{\text{brain}}} P_{d,\text{brain}}(\boldsymbol{r}) dV_{\text{brain}}}{\int_V P_d(\boldsymbol{r}) dV}, \quad V_{\text{brain}} \subset V. \tag{5}$$

The design optimization is based on a parametric analysis (see Table II) that aims to maximize efficiency as well as bandwidth (Δf) of the receive antenna (see Table III). The band is chosen based on the constraint $S_{11} \leq -10$ dB, in order to minimize the mismatch (S_{11}) between antenna and tissue load. For convenience, we define $\eta_{\Delta f}$ as the average efficiency over Δf where $S_{11} \leq -10$ dB. This function $(\eta_{\Delta f})$ is used to quantitatively compare simulation results of the different parametric analyses. Furthermore, due to the frequency allocation for wireless local area networks, mobile phones, and pagers, by the Federal Communications Commission (FCC), some frequency bands must be avoided due to excessive environmental background interference (see Table III).

E. Radiometric Temperature Measurements

Following the design optimization, the antenna was fabricated, connected to the radiometer electronics described elsewhere [11], [24], [25] and tested on the physical phantom. The radiometer used is an analog Dicke radiometer that uses a dual-matched ultralow noise and high-gain (G) amplifier design to provide a time-sequenced comparison to an internal 50-Ω reference for long-term stable calibration. Radiometric power (P_{ant}) was measured continuously and converted into an equivalent temperature (T_B) using

$$P_{\text{ant}} = G k_B T_B \Delta f \tag{6}$$

where k_B is the Boltzmann constant. Volume averaged brain temperature (T_{brain}) was extracted from T_B using an algorithm similar to those described previously [9]–[11], [14] and modified for this application by Maccarini *et al.* [25]:

$$T_B = \alpha_1 T_{\text{brain}} + \alpha_2 T_{\text{ref}}, \quad \alpha_2 = 1 - \alpha_1 \tag{7}$$

where $\alpha_i (i = 1, 2)$ are calibration coefficients determined from a calibration measurement and (6); T_{ref} is the temperature of the 50-Ω calibration reference that is being monitored with a thermistor located in the printed circuit board. This reference temperature allows to derive the gain in (6) since the amplifiers of the reference and antenna are matched, yielding $P_{\text{ref}} = G k_B T_{\text{ref}} \Delta f$.

An initial steady-state condition was established in the head physical model by circulating the scalp phantom at 32 °C and brain phantom at 37 °C. Temperature in the brain phantom was cycled between the values 37–27–37 °C to simulate the induction of hypothermia during surgery. The heating water bath for the scalp phantom was held constant to provide constant scalp temperature and thus ensuring radiometric reading variations independent from scalp. All phantom temperatures were monitored continuously using fiber-optic probes (Luxtron 3100, LumaSense Technologies, Santa Clara, CA, USA) for comparison with the radiometric readings.

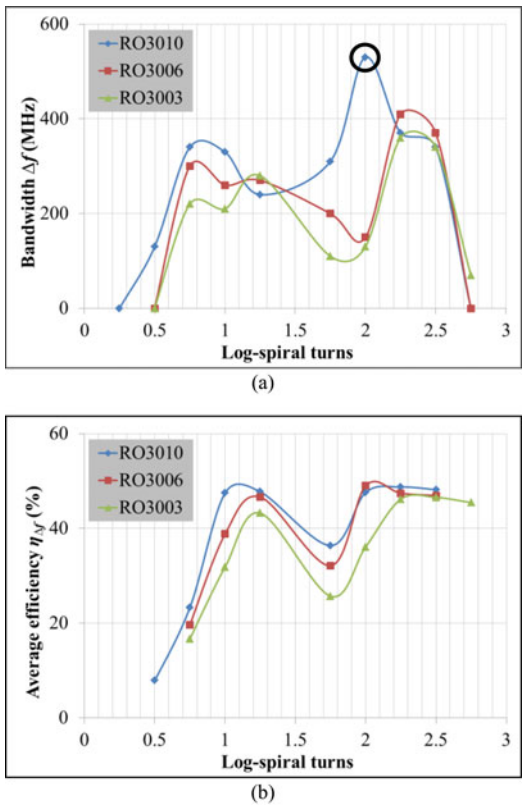

Fig. 5. Determination of operating frequency bandwidth Δf where $S_{11} \leq -10$ dB for substrates RO3010 $(\varepsilon_{r,\text{substrate}} = 10.2)$, RO3006 $(\varepsilon_{r,\text{substrate}} = 6.15)$ and RO3003 $(\varepsilon_{r,\text{substrate}} = 3)$: (a) Δf versus log-spiral turns N and (b) average antenna efficiency $\eta_{\Delta f}$ versus N. Nominal values: $\delta = 1$ mm and $\varepsilon_{r,\text{coverlay}} = 30$.

III. RESULTS AND DISCUSSION

A. Antenna Bandwidth Simulations

Simulations of S_{11} and efficiency (η) showed no significant dependence on coverlay permittivity over the range 5–40; thus, simulations were performed using $\varepsilon_{r,\text{coverlay}} = 30$ due to availability. For the initial optimization of $\varepsilon_{r,\text{substrate}}$, simulations used $\delta = 1$ mm since that parameter as found to be less critical than $\varepsilon_{r,\text{substrate}}$ and number of turns N [18]. After determining optimal $\varepsilon_{r,\text{substrate}}$ and N, a parametric analysis for δ was implemented in order to refine the results.

Fig. 5(a) presents operating bandwidth Δf for which $S_{11} \leq -10$ dB and compares simulation results for three substrates (see Table I). Best results are achieved for substrate RO3010 with $N = 2$, which provides an ultrawideband of approximately

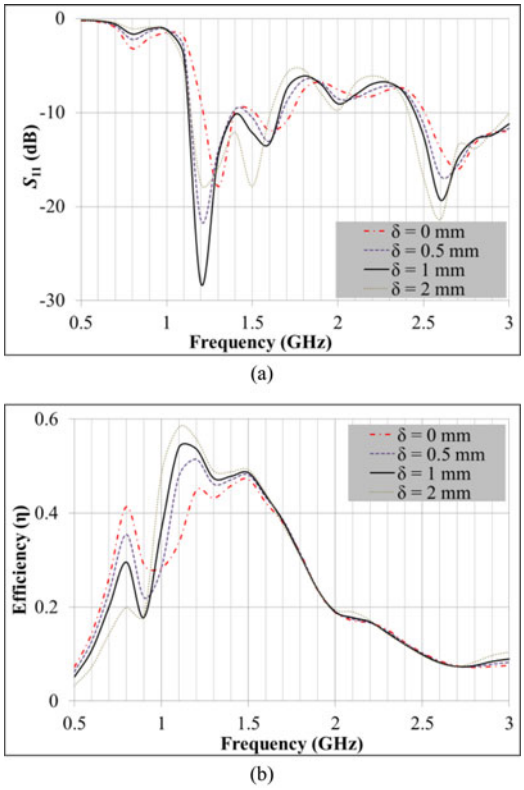

Fig. 6. Coverlay thickness (δ) parametric analysis to improve impedance matching at the interface between antenna and human head. (a) S_{11} versus frequency and (b) antenna efficiency versus frequency. Nominal values: $N = 2, \varepsilon_{r,\text{coverlay}} = 30$ and $\varepsilon_{r,\text{substrate}} = 10.2$.

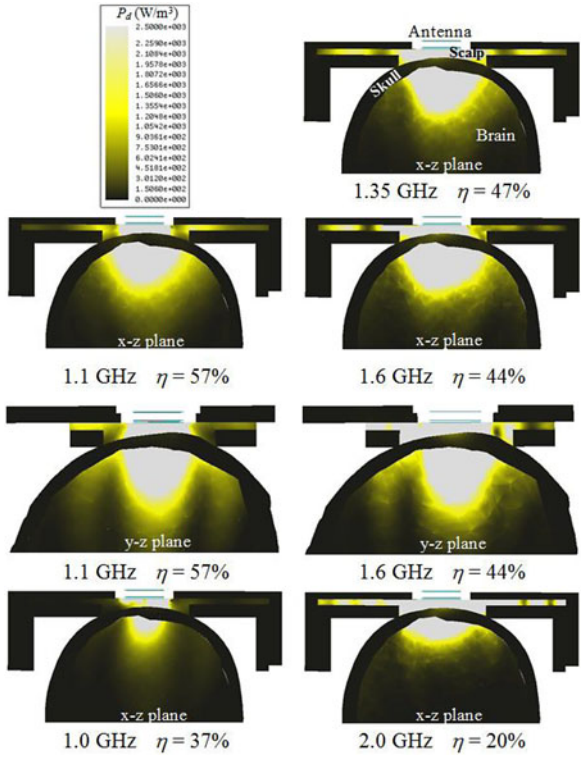

Fig. 7. HFSS-simulated receive pattern for the 2.5-cm log-spiral antenna when placed on the heterogeneous multilayer human head model. The receive pattern is shown for five specific radiometric sensing frequencies, i.e., 1.0, 1.1, 1.35, 1.6, and 2.0 GHz. Radiometric antenna efficiency η (%) is evaluated in terms of the ratio of the power collected from brain to the total power received by the antenna and thus intrinsically normalized.

500 MHz. Fig. 5(b) presents average antenna efficiency across the band ($\eta_{\Delta f}$), showing similar efficiencies for RO3010 and RO3006 substrates for most values of N and generally higher efficiency with increasing substrate permittivity. Due to the combination of high efficiency and large bandwidth, $\varepsilon_{r,\text{substrate}} = 10.2$ (RO3010) and N=2 are chosen as nominal values for the remaining simulations.

The use of a coverlay improves both the matching impedance and antenna efficiency (see Fig. 6). Best results for S_{11} and efficiency are achieved for $\delta = 1$ mm [see Fig. 6(a)] yielding an average efficiency $\eta_{\Delta f}$ of 50.3% in the 1.1–1.6 GHz band [see Fig. 6(b)]. Note that the difference between the higher and lower frequencies of this band corresponds to the Δf highlighted with a circle in Fig. 5(a). Antenna efficiency results are only presented for the coverlay thickness parametric analysis since it does not vary significantly in the remaining variables' sweeps. In fact, the efficiency is higher than 40% across the band where $S_{11} \leq -10$ dB for all simulations, with the exception of the zero thickness coverlay [see Fig. 6(b)].

B. Simulated Radiation Patterns

Fig. 7 shows the power loss density $P_d(\text{W/m}^3)$ of the optimized tapered log-spiral antenna for five representative frequencies. Within the range 1.1–1.6 GHz, simulations demonstrate that a significant portion of the MW energy is received from deep brain. As expected, there is little power deposited in (or received from) the phantom bone due to its very low electrical conductivity (Fig. 4). Below 1.0 GHz, the antenna exhibits lower efficiency due to its small size compared to the wavelength, though this improves immunity from EMI at the particularly noisy 810–960 MHz band. At higher frequencies approaching 2.0 GHz, energy received by the antenna is collected mainly from the scalp.

The lower cutoff frequency f_L can be extrapolated from Fig. 6(a) and corresponds to the frequency where S_{11} starts decreasing abruptly: $f_L = 0.98$ GHz. From (3), we can deduce $\varepsilon_{r,\text{eff}} = 15.2$, which is slightly higher than $\varepsilon_{r,\text{substrate}} = 10.2$. The higher effective permittivity occurs since it also accounts for higher scalp and brain phantom permittivities (see Fig. 4), e.g., $\varepsilon_{\text{r,scalp}} = 67.0$ and $\varepsilon_{r,\text{brain}} = 59.0$ at 1.35 GHz. These results indicate that the substrate dictates the wavelength attenuation of the electromagnetic waves that are detected by the spiral antenna. Using $\varepsilon_{r,,\text{eff}} = 15.2$, one can estimate the detectable wavelengths by the spiral antenna to be in the interval 48.1–70.0 mm along the bandwidth 1.1–1.6 GHz. These values are higher, but of the same order, than the spiral length 41.2 mm ($N = 2$). The radiation patterns on Fig. 7 (xz and yz planes) for the lower (1.1 GHz) and upper (1.6 GHz) frequencies of the operating band show a slightly more focused radiation pattern in the yz plane which indicates an elliptical polarization.

Fig. 8 presents HFSS simulations of absolute power collected from different regions of the head model as a function of

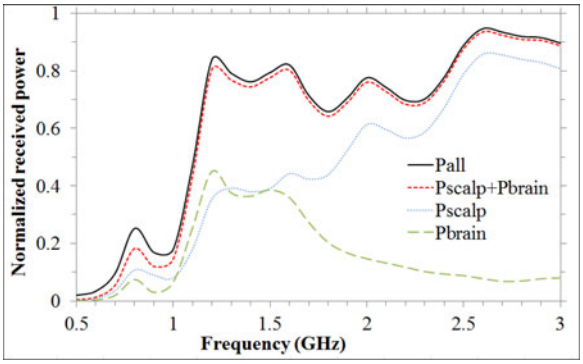

Fig. 8. Normalized received power versus frequency. From brain (Pbrain), scalp (Pscalp), sum of power received from scalp and brain (Pscalp+Pbrain), and from the entire computational volume composed of air, scalp, skull, brain, and head model plexiglass support structure (Pall).

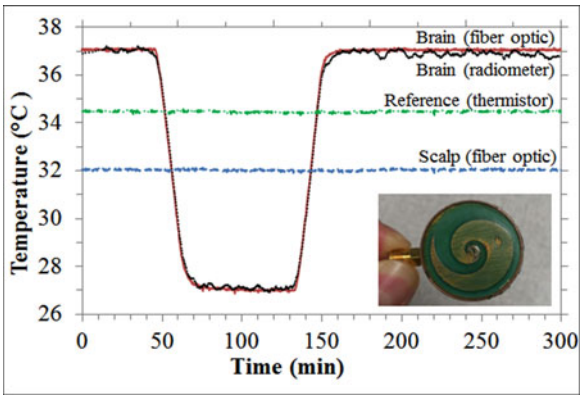

Fig. 9. Effective brain temperature derived from total power measurements of the noninvasive radiometric sensor (black curve) closely mirrors the actual temperature of the circulating brain phantom (red curve). Green curve (dash dot line) shows reference temperature and blue curve (dash line) shows the measured scalp temperature, with no significant drift during the 4.5-h period of monitoring. Bottom right: photo of a 2.5-cm-diameter log-spiral antenna encapsulated together with radiometer printed circuit inside a cylindrical copper tube with 1-mm wall thickness and 1.5-cm height.

frequency. One can observe that the antenna receives energy mainly from scalp and brain in the 1.1–1.6 GHz band and mainly from scalp at higher frequencies. The remaining energy is collected from skull ($<0.3\%$), mylar, and plexiglass used to support the head phantom ($<1.5\%$), and the antenna materials including substrate and coverlay ($<2.3\%$).

C. Antenna Implementation and Phantom Results

A radiometer sensor was built according to the optimized parameters (bottom right in Fig. 9). The sensor package is lightweight and has a low profile of 2.8 cm diameter by 1.5 cm height. This sensor can be held in place on the scalp with an EMI shielding adhesive patch and/or elastic strap. The sensor was tested in a realistic head phantom experiment that simulates brain temperature variations over a 4.6-h surgery. Radiometric brain temperature ($T_{\rm brain}$) was determined using (6) and (7) with $\alpha_1 = 0.32$, which was determined from an initial calibration measurement ($T_{\rm brain} = 37\ ^\circ{\rm C}$ at $t = 0$ s). The α coefficients are, in theory, closely related to the average thermal radiation contribution from each region over the band 1.1–1.6 GHz. For instance, one could expect $\alpha_1 \approx 0.5$ since in brain $\eta_{\Delta f} \approx 50\%$, but in practice the radiometer system components also contribute with thermal radiation, which reduces the overall contribution from phantom materials. From simulations, the energy collection is mostly from scalp and brain. Equation (7) accounts for brain temperature explicitly, whereas scalp temperature is embodied in $T_{\rm ref}$ since the high thermal conductivity ($>1{\rm W/m/K}$) of both coverlay and substrate materials allow high heat transfer between scalp substrate, where the thermistor is located. This is clearly illustrated in Fig. 9, since $T_{\rm ref}$ is dictated by $T_{\rm scalp}$ plus 2.4 °C due to electronic heating.

The scalp phantom was maintained constant at 32 °C to demonstrate clearly that the radiometric power changes were due entirely to intracranial temperature variation. However, during surgery, all tissues reduce their temperature due to anesthesia. The next step will be to vary scalp phantom temperature as well, to account for all possible temperature distribution scenarios during surgery. This will imply to refine the calibration algorithm by including explicitly scalp temperature in (7) as $\alpha_3 T_{\rm scalp}$, which will be measured with a thermistor at the skin surface. This setup will allow us to correlate α parameters [see (7)] with simulated average efficiencies ($\eta_{\Delta f}$) and thus isolating the thermal noise contribution of the radiometric system.

The maximum difference between the temperature measured directly with fiber-optic sensors and the calculated equivalent radiometric brain temperature was 0.38 °C during the rapid temperature changes when cooling (−0.35 °C/min) and rewarming (0.32 °C/min) the brain phantom (see Fig. 9). This occurs due to the 74 s delay in measurements caused by a moving median calculation to reduce EMI. However, the temperature rates of patients undergoing surgery are at least ten times slower than the cooling/rewarming rates implemented in our study [7]. Thus, the transient temperature errors during rapid cooling and rewarming periods appear to overestimate the errors of slowly changing temperatures. Moreover, these temperature errors should be lower than the errors from reading core temperature from slowly changing sites like esophagus and rectum. The 0.4 °C experimental error fits the current clinical need of $\leq$0.5 °C resolution, corresponding to the smallest temperature difference that has been associated with hypothermia-induced complications [7]. The data also demonstrate our ability to track temperature changes of brain (core temperature) during long time periods typical of open heart bypass surgery, enabling the physician to carefully monitor and return the patient's temperature to normothermic range quickly at the end of a long procedure.

The presented experimental model of the human head accounts for the major physiological and anatomical parameters but has some limitations. Phantoms never reproduce the actual clinical situation precisely. Brain, in particular, is a complex organ with spatial and temporal temperature variations that cannot be predicted and may degrade the accuracy of volume averaged clinical measurements. Despite some limitations, the head phantom described in this study serves a dual purpose. 1) to validate the computational method used to design the MW antenna and 2) to test accuracy and long-term stability of the radiometric system linked to the antenna. Furthermore, a new computational

model is currently under implementation in order to refine the design of the antenna for clinic use. This virtual model incorporates human electrical properties and accounts for more detailed anatomy that includes skin, scalp, meninges, cerebrospinal fluid, and brain parenchyma.

IV. Conclusion

An MW radiometric sensor was developed for rapid noninvasive measurement of brain temperature. The key element of the sensor is a tapered 2.5-cm-diameter microstrip log-spiral antenna, embedded in a 2.8-cm-diameter low-cost radiometric sensor. The antenna design was optimized for deep brain sensing yielding a log-spiral antenna with $N = 2, \delta = 1\ \mathrm{mm}, \varepsilon_{r,\mathrm{coverlay}} = 30$ and $\varepsilon_{r,\mathrm{substrate}} = 10.2\,(\mathrm{RO3010})$ over the 1.1–1.6 GHz band. This particular arrangement allows a theoretical bandwidth $\Delta f = 500$ MHz and an average antenna efficiency of 50.3% over the optimized band. These simulations allow estimation of the different received energy contributions from scalp, skull, and brain tissues, which pave the way for temperature profiling across the human head. The sensor was tested on a full-scale multilayer tissue phantom of the human head. During a 4.5-h experiment, the maximum error associated with the calculated radiometric brain temperature was 0.4 °C. We anticipate that this newly developed sensor will help reduce complications from extended surgeries, thereby reducing overall costs and improving clinical outcomes for patients recovering from post-surgical hypothermia.

Acknowledgment

The authors would like to thank ANSYS and Agilent for the continuous software support.

References

[1] K. H. Polderman, "Mechanisms of action, physiological effects, and complications of hypothermia," *Crit. Care Med.*, vol. 37, no. 7, pp. S186–S202, Jul. 2009.

[2] T. D. Yan, P. G. Bannon, J. Bavaria, J. S. Coselli, J. A. Elefteriades, R. B. Griepp, G. C. Hughes, S. A. Lemaire, T. Kazui, N. T. Kouchoukos, M. Misfeld, F. W. Mohr, A. Oo, L. G. Svensson, and D. H. Tian, "Consensus on hypothermia in aortic arch surgery," *Ann. Cardiothoracic Surg.*, vol. 2, no. 2, pp. 163–168, Mar. 2013.

[3] S. Rajagopalan, E. Mascha, J. Na, and D. I. Sessler, "The effects of mild perioperative hypothermia on blood loss and transfusion requirement," *Anesthesiology*, vol. 108, no. 1, pp. 71–77, Jan. 2008.

[4] M. Schwarz, M. W. Krueger, H. J. Busch, C. Benk, and C. Heilmann, "Model-based assessment of tissue perfusion and temperature in deep hypothermic patients," *IEEE Trans. Biomed. Eng.*, vol. 57, no. 7, pp. 1577–1586, Jul. 2010.

[5] J. L. Moran, J. V. Peter, P. J. Solomon, B. Grealy, T. Smith, W. Ashforth, M. Wake, S. L. Peake, and A. R. Peisach, "Tympanic temperature measurements: Are they reliable in the critically ill? A clinical study of measures of agreement," *Crit. Care Med.*, vol. 35, no. 1, pp. 155–164, Jan. 2007.

[6] L. Lawson, E. J. Bridges, I. Ballou, R. Eraker, S. Greco, J. Shively, and V. Sochulak, "Accuracy and precision of noninvasive temperature measurement in adult intensive care patients," *Amer. J. Crit. Care*, vol. 16, no. 5, pp. 485–496, Sep. 2007.

[7] D. I. Sessler, "Temperature monitoring and perioperative thermoregulation," *Anesthesiology*, vol. 109, no. 2, pp. 318–338, Aug. 2008.

[8] L. McIlvoy, "Comparison of brain temperature to core temperature: A review of the literature," *J. Neurosci. Nurs.*, vol. 36, no. 1, pp. 23–31, Feb. 2004.

[9] K. Maruyma, S. Mizushina, T. Sugiura, G. M. J. Van Leeuwen, J. W. Hand, G. Marrocco, F. Bardati, A. D. Edwards, D. Azzopardi, and D. Land, "Feasibility of noninvasive measurement of deep brain temperature in newborn infants by multifrequency microwave radiometry," *IEEE Trans. Microw. Theory Tech.*, vol. 48, no. 11, pp. 2141–2147, Nov. 2000.

[10] S. Jacobsen and P. R. Stauffer, "Non-parametric 1-D temperature restoration in lossy media using Tikhonov regularization on sparse radiometry data," *IEEE Trans. Biomed. Eng.*, vol. 50, no. 2, pp. 178–188, Feb. 2003.

[11] K. Arunachalam, P. R. Stauffer, P. F. Maccarini, S. Jacobsen, and F. Sterzer, "Characterization of a digital microwave radiometry system for noninvasive thermometry using a temperature-controlled homogeneous test load," *Phys. Med. Biol.*, vol. 53, no. 14, pp. 3883–3901, Jul. 2008.

[12] F. Bardati and S. Iudicello, "Modeling the visibility of breast malignancy by a microwave radiometer," *IEEE Trans. Biomed. Eng.*, vol. 55, no. 1, pp. 214–221, Jan. 2008.

[13] L. Dubois, J. P. Sozanski, V. Tessier, J. C. Camart, J. J. Fabre, J. Pribetich, and M. Chive, "Temperature control and thermal dosimetry by microwave radiometry in hyperthermia," *IEEE Trans. Microw. Theory Tech.*, vol. 44, no. 10, pp. 1755–1761, Oct. 1996.

[14] S. Jacobsen and P. R. Stauffer, "Can we settle with single-band radiometric temperature monitoring during hyperthermia treatment of chestwall recurrence of breast cancer using a dual-mode transceiving applicator?" *Phys. Med. Biol.*, vol. 52, no. 4, pp. 911–928, Feb. 2007.

[15] S. Jacobsen, P. R. Stauffer, and D. G. Neuman, "Dual-mode antenna design for microwave heating and noninvasive thermometry of superficial tissue disease," *IEEE Trans. Biomed. Eng.*, vol. 47, no. 11, pp. 1500–1509, Nov. 2000.

[16] A. Oikonomou, I. S. Karanasiou, and N. K. Uzunoglu, "Phased-array near field radiometry for brain intracranial applications," *Prog. Electromagn. Res.*, vol. 109, pp. 345–360, Oct. 2010.

[17] K. Arunachalam, P. F. Maccarini, V. De Luca, F. Bardati, B. W. Snow, and P. R. Stauffer, "Modeling the detectability of vesicoureteral reflux using microwave radiometry," *Phys. Med. Biol.*, vol. 55, no. 18, pp. 5417–5435, Sep. 2010.

[18] Y. Birkelund, O. Klemetsen, S. K. Jacobsen, K. Arunachalam, P. Maccarini, and P. R. Stauffer, "Vesicoureteral reflux in children: A phantom study of microwave heating and radiometric thermometry of pediatric bladder," *IEEE Trans. Biomed. Eng.*, vol. 58, no. 11, pp. 3269–3278, Nov. 2011.

[19] D. B. Rodrigues, P. F. Maccarini, S. Salahi, E. Colebeck, E. Topsakal, P. J. S. Pereira, P. Limao-Vieira, and P. R. Stauffer, "Numerical 3D modeling of heat transfer in human tissues for microwave radiometry monitoring of brown fat metabolism," *Proc. SPIE*, vol. 8584, pp. 0S1–12, Feb. 2013.

[20] J. D. Dyson, "The equiangular spiral antenna," *IRE Trans. Ant. Prop.*, vol. AP-7, no. 2, pp. 181–187, Apr. 1959.

[21] R. H. Duhamel and D. E. Isbell, "Broadband logarithmically periodic antenna structures," *Proc. Int. Conv. Rec. Inst. Rad. Eng.*, vol. 45, no. 3, pp. 119–128, 1957.

[22] J. A. Kaiser, "The Archimedean two-wire spiral antenna," *IRE Trans. Ant. Prop.*, vol. 8, no. 3, pp. 312–323, May 1960.

[23] S. Gabriel, R. W. Lau, and C. Gabriel, "The dielectric properties of biological tissues: III. Parametric models for the dielectric spectrum of tissues," *Phys. Med. Biol.*, vol. 41, no. 11, pp. 2271–2293, Nov. 1996.

[24] O. Klemetsen, Y. Birkelund, S. K. Jacobsen, P. F. Maccarini, and P. R. Stauffer, "Design of medical radiometer front-end for improved performance," *Prog. Electromagn. Res. B*, vol. 27, pp. 289–306, Jan. 2011.

[25] P. F. Maccarini, D. B. Rodrigues, T. R. Oliveira, and P. R. Stauffer, "Radiometric profiling for brain temperature monitoring," *IEEE Sens. J.*, to be published.

Authors' photographs and biographies not available at the time of publication.